Transferability of Labels Between Multilens Cameras

Ignacio de Loyola Páez-Ubieta[a], Daniel Frau-Alfaro[b] and Santiago T. Puente[c]

AUtomatics, RObotics, and Artificial Vision (AUROVA) Lab, University Institute for Computer Research (IUII), University of Alicante, Crta. San Vicente s/n, San Vicente del Raspeig, E-03690, Alicante, Spain

Keywords: Multispectral Imagery, Labeling, Phase Correlation, Label Transfer, Pills.

Abstract: In this work, a novel approach for the automated transfer of Bounding Box (BB) and mask labels across different channels on multilens cameras is presented. For that purpose, the proposed method combines the well-known phase correlation method with a refinement process. In the initial step, images are aligned by localising the peak of intensity obtained in the spatial domain after performing the cross-correlation process in the frequency domain. The second step consists of obtaining the optimal transformation through an iterative process that maximises the IoU (Intersection over Union) metric. The results show that the proposed method enables the transfer of labels across different lenses on a camera with an accuracy of over 90% in the majority of cases, with a processing time of just 65 ms. Once the transformations have been obtained, artificial RGB images are generated for labelling purposes, with the objective of transferring this information into each of the other lenses. This work will facilitate the use of this type of camera in a wider range of fields, beyond those of satellite or medical imagery, thereby enabling the labelling of even invisible objects in the visible spectrum.

1 INTRODUCTION

The training of a detection (Wang et al., 2023) or segmentation (Wang et al., 2020) Neural Network (NN) requires a large amount of data to adapt an already trained model to a specific task. This is exemplified by the training of a NN to detect or segment household waste (Páez-Ubieta et al., 2023) (Páez-Ubieta et al., 2023).

However, recent developments have witnessed the advent of automated labeling models for objects in RGB images. Notably, the Segment Anything Model (SAM) model (Kirillov et al., 2023) has rapidly ascended to become a standard reference in this field.

Multi-Spectral Imaging (MSI) is a technique that employs sensors capable of generating images at different frequency ranges compared to those produced by traditional RGB cameras. In a multitude of disciplines, including agriculture (Hoffer et al., 1966) (Mia et al., 2023), medicine (Andersson et al., 1987) (Ma et al., 2023) and remote sensing (Maxwell, 1976) (Yuan et al., 2021), these cameras have demonstrated considerable potential over the past few decades.

However, traditional computer vision techniques for detecting and segmenting objects have relied on RGB images, excluding other perception sensors such as Light Detection And Ranging (LiDAR) or multilens cameras. Nevertheless, an increasing number of articles utilising sensors other than RGB cameras for labeling purposes are being published (Ošep et al., 2024) (Gallagher et al., 2024).

For instance, (Gómez and Meoni, 2021) introduced a semi-supervised learning approach for the automatic classification of multispectral scenes derived from land datasets, including EuroSAT (Helber et al., 2019) and the aerial UC Merced land use (UCM) (Yang and Newsam, 2010). For that purpose, they label between 5 and 300 images per class, which are then fed into a Graphics Processing Unit (GPU) for training in order to obtain a model that is capable of generalization. In our case, a training phase is not required, as the transformation between the camera lenses is directly obtained. In this way, more detailed object recognition is possible, rather than just scene classification. Furthermore, 15 images were used during the transformation phase; nonetheless, the proposed method is also able to make use of a smaller number of images.

Another example is provided by (Ulku et al., 2022), in which the authors seek to segment trees semantically using satellite and aerial images from

[a] https://orcid.org/0000-0001-9901-7264

[b] https://orcid.org/0009-0000-4098-3783

[c] https://orcid.org/0000-0002-6175-600X

Páez-Ubieta, I. L., Frau-Alfaro, D. and Puente, S. T.
Transferability of Labels Between Multilens Cameras.
DOI: 10.5220/0013154100003912
In *Proceedings of the 20th International Joint Conference on Computer Vision, Imaging and Computer Graphics Theory and Applications (VISIGRAPP 2025) - Volume 3: VISAPP*, pages 410-417
ISBN: 978-989-758-728-3; ISSN: 2184-4321

the DSTL Satellite Imagery Feature Detection Image (Benjamin et al., 2016) and RIT-18 (The Hamlin State Beach Park) Aerial Image (Kemker et al., 2018) datasets. To this end, the authors use several segmentation NNs to perform the task of labeling trees on the images. In constrast, our approach does not require any kind of semantic segmentation NNs to label our images. Additionally, the trees in the images used by the authors cover a significant portion of the image, which facilitates the NN's task of identifying and labeling them. In comparison, the objects in our case are much smaller, making it more challenging.

Other works, such as (Park et al., 2021), use multispectral and RGB cameras to detect sick pine trees through the analysis of aerial photographs. In order to align the images for subsequent labeling, the Scale-Invariant Feature Transform (SIFT) method (Lowe, 1999) is employed. However, this aforementioned method is only viable when keypoints and descriptors can be extracted from the images. It is therefore not applicable to uniform objects, which can be addressed by our method. Furthermore, the NN analyses both RGB and 6 channel multispectral images, which is an inefficient process given that some of the 9 channels may contain no information at all.

The following work aims to obtain the transformation between images captured from a multispectral multilens camera. The final objective is to facilitate the transfer of Bounding Box (BB) or mask labels from one image to the others. Additionally, the system enables users to label objects with minimal effort in RGB images, thereby reducing the time required for this task. The generation of these RGB images requires the combination of the appropriate frequencies from the multispectral camera in the correct sequence. In order to obtain the transformation, it is requisite to calculate the displacement using the frequency domain and refine it progressively in order to obtain the optimal result using just Central Processing Unit (CPU) resources. The exclusion of GPUs will enable the utilisation of more economical computing devices, while simultaneously reducing energy consumption.

The main contributions of this work are:

- A new method for obtaining the transformation between the lens of a multispectral camera, which has been demonstrated to be highly accurate.
- The possibility of generating fake RGB images from combining its components by applying the aforementioned transform.
- Transforming labels in both BB and mask formats across images is conducted in order to label objects that disappear in certain frequencies.

This work is organised as follows: Section 2 introduces the proposed method, which is divided into two steps, Section 3 presents the setup that is used for experiments, as well as the transformations between the lens and the fake RGB labeling process and Section 4 summarises the article and further work using this method as a core project.

2 METHODOLOGY

This Section details the method for obtaining the transformation between different lenses on the camera. It is composed of two steps: firstly, the displacement is calculated using the phase correlation method; secondly, the result is refined using a sliding window across several scales.

2.1 Displacement Calculation

The lenses of a multilens multispectral camera are not aligned, resulting in images that are not aligned. Given that the lenses are at the same height, it can be reasonably assumed that a two-dimensional transformation (rotation, translation, scale and/or skew) is the most probable conversion to relate them. The aforementioned assumption, positing a mere displacement between the captured images by the disparate lenses, was made. However, should the results prove otherwise, an alternative transformation would be utilized. This could include the log-polar transform for addressing rotations and scale estimation, or an affine parameter estimation in instances where skew transformations are to be dealt with.

The images obtained are in the space domain, wherein each pixel represents the intensity. However, we move to the frequency domain, in which images are reorganised according to frequency, with the distribution of frequencies determined by their periodicity. High periodicity is represented in the centre of the image, while low periodicity is represented far from it.

By taking advantage of the distribution of images in the frequency domain, the displacement between two images can be expressed as a linear phase change. This is the fundamental concept underlying the phase correlation algorithm.

The algorithm receives two images, i_1 and i_2, as input. The first step is to remove sharp discontinuities at the image borders, as their presence results in the generation of a high-frequency component, thereby reducing the accuracy of the method. This issue is known as spectral leakage. However, the use of a Hanning window (Eq. 1) effectively addresses this problem, resulting in a smoother image with the removal of undesirable artifacts and edges.

$$w(x,y) = \left(0.5\left(1 - cos\left(\frac{2\pi x}{M-1}\right)\right)\right) \cdot \left(0.5\left(1 - cos\left(\frac{2\pi y}{N-1}\right)\right)\right) \tag{1}$$

where M and N represent the dimensions of the image, while x and y represent the pixel coordinates. Upon application to the previously referenced images, the resulting values are $i_{1h}(x,y)$ and $i_{2h}(x,y)$, respectively. The second step involves transforming the previously obtained spectral leakage-free images into the frequency domain. This is achieved through by use of the Discrete Fourier Transform (DFT), as illustrated by Eq. 2, which yields $I_{1h}(u,v)$ and $I_{2h}(u,v)$, respectively.

$$I_{1h}(u,v) = \sum_{x=0}^{M-1}\sum_{y=0}^{N-1} i_{1h}(x,y) \cdot e^{-2\pi i\left(\frac{ux}{M}+\frac{vy}{N}\right)} \tag{2}$$

Once the images have been transformed into the frequency domain, the phase shift between them represents the translational shift in the space domain that corresponds to the searched parameter. In order to achieve this, the third step is to isolate the phase information by utilising the cross-power spectrum (Eq. 3), normalising the magnitude and retaining the phase information.

$$CP(u,v) = \frac{I_{1h}(u,v) \cdot I_{2h}^{*}(u,v)}{\left|I_{1h}(u,v) \cdot I_{2h}^{*}(u,v)\right|} \tag{3}$$

where $I_{2h}^{*}(u,v)$ represents the complex conjugate of $I_{2h}(u,v)$. The forth step involves returning to the spatial domain by applying the Inverse Discrete Fourier Transform (IDFT) to the calculated cross-power spectrum, $CP(u,v)$, to obtain the correlation matrix, $c(x,y)$ (Eq. 4).

$$c(x,y) = \sum_{u=0}^{M-1}\sum_{v=0}^{N-1} CP(u,v) \cdot e^{2\pi i\left(\frac{ux}{M}+\frac{vy}{N}\right)} \tag{4}$$

At last, the peak location $(\Delta x, \Delta y)$ in the correlation matrix $c(x,y)$ is identified (Eq. 5) by carrying out a 5×5 weighted centroid operation around the peak, in order to achieve subpixel accuracy. The result is then normalised between 0 and 1.

$$(\Delta x, \Delta y) = weightedCentroid\{\arg\max_{(x,y)}\{c(x,y)\}\} \tag{5}$$

2.2 Refinement

Once the relative displacement $(\Delta x, \Delta y)$ between the two input images, i_1 and i_2, has been obtained using the phase correlation method, a refinement process is required in order to refine the transformation.

In order to achieve this, a series of alternative, potentially improved displacement values are identified. Firstly, the coordinates $(\Delta x, \Delta y)$ are rounded and then added or subtracted a value $RV : i \in 1 \ldots n$, with n representing the number of refinement steps along both both the x and y axes at different scales s. The aforementioned variable s will represent different orders of magnitude, with the discrete values on $[1, 0.1, 0.01]$ varying in order to check pixel and subpixel precision (Eq. 6). This will result in several possible combinations.

$$\begin{aligned} \Delta x_p &= [\Delta x - RV \cdot s, \cdots, \Delta x, \cdots \Delta x + RV \cdot s] \\ \Delta y_p &= [\Delta y - RV \cdot s, \cdots, \Delta y, \cdots \Delta y + RV \cdot s] \end{aligned} \tag{6}$$

The potential values $(\Delta x_p, \Delta y_p)$ are incorporated into a homogeneous transformation (Eq. 7) and applied to the different labels on the image to determine whether a better solution is obtained. To this end, some labelled images are used as a basis for comparison with these newly obtained labels.

$$\begin{bmatrix} l_{N:nx} \\ l_{N:ny} \end{bmatrix} = \begin{bmatrix} 1 & 0 & \Delta x_p \\ 0 & 1 & \Delta y_p \end{bmatrix} \begin{bmatrix} l_{nx} \\ l_{ny} \end{bmatrix} \tag{7}$$

The labels $l = [(l_{1x}, l_{1y}), \ldots, (l_{nx}, l_{ny}), \ldots, (l_{Nx}, l_{Ny})]$ comprise a set of N points that collectively define the boundaries of a labeled objects. In the context of a mask, the value of N may be any positive integer. Alternatively, a BB is defined by $N = 2$, representing the top left and bottom right coordinates of the box.

The final transform will convert the original mask or BB coordinates (l_{nx}, l_{ny}) into the new reference frame, obtaining $l_M = [(l_{M:1x}, l_{M:1y}), \ldots, (l_{M:nx}, l_{M:ny}), \ldots, (l_{M:Nx}, l_{M:Ny})]$. The aforementioned labelled image $l_{GT} = [(l_{GT:1x}, l_{GT:1y}), \ldots, (l_{GT:nx}, l_{GT:ny}), \ldots, (l_{GT:Nx}, l_{GT:Ny})]$ will be compared against the resulting images in order to achieve the highest Intersection Over Union (IOU).

The IOU, also known as the Jaccard index, is a metric that quantifies the degree of overlap between two labels, with a value between 0 and 1. It is represented by Eq. 8.

$$IoU = \frac{l_M \cap l_{GT}}{l_M \cup l_{GT}} \tag{8}$$

3 EXPERIMENTATION

In this Section, a description the hardware and software setup is provided, as well as an overview of the experiments that demonstrate the success of the proposed method for obtaining labels across multiple multispectral images.

3.1 Setup

In terms of the hardware used (see Fig. 1), a MicaSense RedEdge-MX Dual multispectral camera was utilised for the acquisition of the images. The camera is comprised of ten individual cameras, divided into two distinct modules, one dedicated to the red spectrum and the other to the blue. This configuration is illustrated in Fig. 1a. A summary of the frequencies associated with each band is provided in Table 1. All 10 bands generate 12-bit images with a resolution of 1280x960. The camera is mounted on the wrist of an Ur5e 6 Degrees of Freedom (DoF) robotic arm, which enables the camera to be positioned with absolute precision in any given location within the space. In terms of positioning, the camera is situated in parallel with a table at a distance of 500 mm (see Fig. 1b). With regard to the objects employed in the experimental procedure, 16 small pills, measuring between 8 and 22 mm are utilised. These provide a diverse range of shapes and colours, necessary for the completion of the planned experiments.

Table 1: Band numbers, frequencies and color names for each channel on the MicaSense RedEdge-MX Dual camera.

Module	Band	f ± A (nm)	Color name
Red	1	475 ± 16	Blue
	2	560 ± 13.5	Green
	3	668 ± 7	Red
	4	717 ± 6	Red Edge
	5	842 ± 28.5	Near IR
Blue	6	444 ± 14	Coastal Blue
	7	531 ± 7	Green
	8	650 ± 8	Red
	9	705 ± 5	Red Edge I
	10	740 ± 9	Red Edge II

In terms of software, images were labeled using the LabelMe tool (Torralba et al., 2010). Two different labeling approximations were employed in all experiments: BB and mask. The computer used to obtain the results operates on the Ubuntu 20.04.4 operating system with Python 3.8.10 and OpenCV 4.7.0 software, running on an 11th Generation Intel© Core™ i9-11900H processor with 8 physical and 16 logical cores, respectively. It operates at a frequency of 2.50 GHz, which is sufficient to perform all necessary operations in a short period of time.

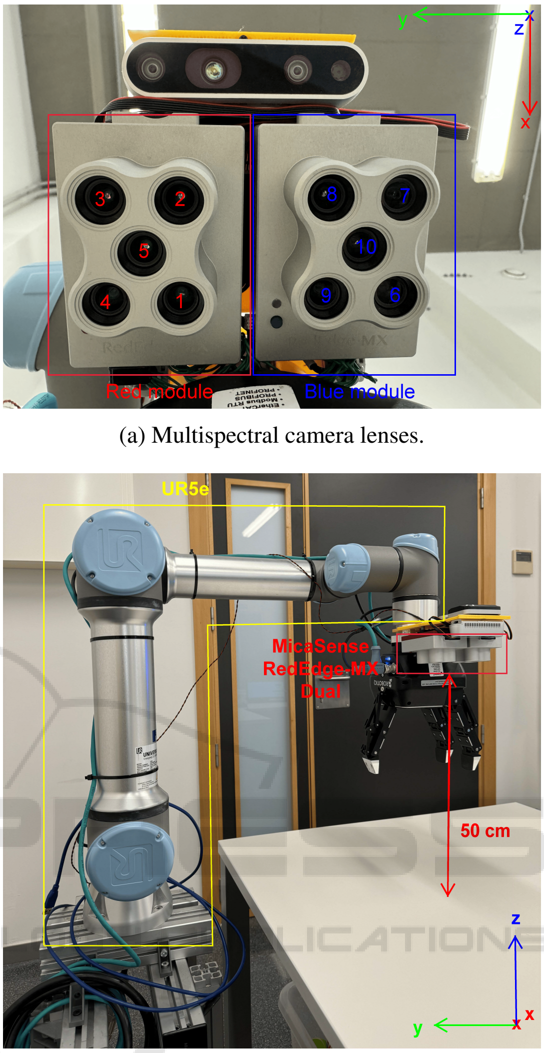

(a) Multispectral camera lenses.

(b) Robotic arm with the MicaSense RedEdge-MX Dual.

Figure 1: Hardware used during the experiments.

3.2 Transformations

Although the camera is equipped with ten lenses, only those situated in the red half of the apparatus will be utilised.

In practice, 15 images were captured with each camera, of which 12 were used to obtain the transform and 3 to verify the accuracy of the obtained transform. The training images from band 5 (lenses in the middle) and the test images from all five lenses were labelled. Additionally, the refinement step n was set to 5, indicating that 121 potential matrices exist at three distinct levels of pixel precision.

Following the application of the phase correlation method and refinement for both BB and mask labels, the results in Tables 2 and 3 were obtained.

Table 2: Transformations in pixel level, IOU and time for BB labels to be transferred from band 5 into the other lenses.

Band	Transform (px)	IoU (%)	Time (ms)
1	${}^1_5T_{BB} = \begin{pmatrix}-52.0\\47.0\end{pmatrix}$	98.58	66.31
2	${}^2_5T_{BB} = \begin{pmatrix}53.9\\46.1\end{pmatrix}$	100	53.52
3	${}^3_5T_{BB} = \begin{pmatrix}52.9\\-23.4\end{pmatrix}$	95.95	55.66
4	${}^4_5T_{BB} = \begin{pmatrix}-52.1\\-18.9\end{pmatrix}$	93.53	56.55

Table 3: Transformations in pixel level, IOU and time for mask labels to be transferred from band 5 into the other lenses.

Band	Transform (px)	IoU (%)	Time (ms)
1	${}^1_5T_{MK} = \begin{pmatrix}-52.05\\47.2\end{pmatrix}$	97.49	82.81
2	${}^2_5T_{MK} = \begin{pmatrix}54.78\\46.52\end{pmatrix}$	94.36	72.58
3	${}^3_5T_{MK} = \begin{pmatrix}53.5\\-23.8\end{pmatrix}$	93.77	73.05
4	${}^4_5T_{MK} = \begin{pmatrix}-53.24\\-19.01\end{pmatrix}$	89.91	58.83

In order to depict the progressive refinement process and its incremental enhancement of the IOU, band 1 from mask labeling is presented in Table 4. Step 0 comprises the application of phase correlation, step 1 involves the refinement of the image at the pixel level with s equal to 1, step 2 entails the refinement of the image at the subpixel level with s equal to 0.1, and step 3 comprises the refinement of the image at two levels of subpixel with s equal to 0.01.

Table 4: Phase correlation and refinement steps applied to band 1 of mask labeled images.

Step	Transform (px)	IoU (%)	Time (ms)
0	${}^1_5T_{MK-0} = \begin{pmatrix}-51.85\\47.02\end{pmatrix}$	96.73	76.75
1	${}^1_5T_{MK-1} = \begin{pmatrix}-52.0\\47.0\end{pmatrix}$	96.99	1.96
2	${}^1_5T_{MK-2} = \begin{pmatrix}-52.0\\47.2\end{pmatrix}$	97.40	2.05
3	${}^1_5T_{MK} = \begin{pmatrix}-52.05\\47.2\end{pmatrix}$	97.49	2.05

The application of ${}^1_5T_{BB}$, ${}^2_5T_{BB}$, ${}^3_5T_{BB}$ and ${}^4_5T_{BB}$, as detailed in Table 2, has resulted in the generation of several labeled images of BB. These can be observed in Fig. 2. As an illustrative example, Fig. 2a is provided, which represents band 5. Once the labels of this image have been transformed, the images in Figs. 2b, 2c, 2d and 2e are generated. As can be observed, the transformed labels are integrated almost perfectly into the objects of the other bands, eliminating the necessity for manual annotation. For a rapid assessment of quality, ground truth human-labeled images are provided in Figs. 2f, 2g, 2h and 2i. The least optimal result is observed in band 4, where the pill's outline begins to merge with the background, making it challenging for both the proposed method and the user to distinguish it.

Proceeding to a more challenging case, the efficacy of mask-labeled images is assessed. The images are transformed using matrices ${}^1_5T_{MK}$, ${}^2_5T_{MK}$, ${}^3_5T_{MK}$ and ${}^4_5T_{MK}$, as detailed in Table 3.The results of the aforementioned process are illustrated in Fig. 3. The layout is consistent with that observed in Fig. 2. In consideration of the aforementioned factors, the most unfavourable outcome is once again band 4. The underlying cause is identical to that observed in the preceding instance. The pill begins to exhibit a noticeable decline in visibility, particularly in comparison to the other three bands. Nevertheless, the labelling process remains successful.

3.3 RGB Label Transferability

Once it has been demonstrated that the labelling process is successful, a further experiment will be conducted. This will involve labelling RGB images created from the multispectral images and then transforming these labels to the other bands.

To this end, the bands representative of the red, green, and blue frequencies must be combined. As indicated in Table 1, bands 1-3 from the red module are the pertinent ones. Consequently, the images are converted from bands 1-3 to band 5 by means of Eq. 9, resulting in an artificial RGB image $im_{RGB} = [R, G, B]$.

$$\begin{aligned} R &=^3_5 \mathrm{T}^{-1}_{BB|mask} \cdot im_{band3} \\ G &=^2_5 \mathrm{T}^{-1}_{BB|mask} \cdot im_{band2} \\ B &=^1_5 \mathrm{T}^{-1}_{BB|mask} \cdot im_{band1} \end{aligned} \tag{9}$$

Subsequently, the user labels the aforementioned RGB image in BB or mask format as $l_{RGB} = [(l_{RGB:1x}, l_{RGB:1y}), \ldots, (l_{RGB:nx}, l_{RGB:ny}), \ldots, (l_{RGB:Nx}, l_{RGB:Ny})]$. Once the label is complete, it is transferred back into the other bands in the camera, thus obtaining labels in all frequencies (Eq. 10).

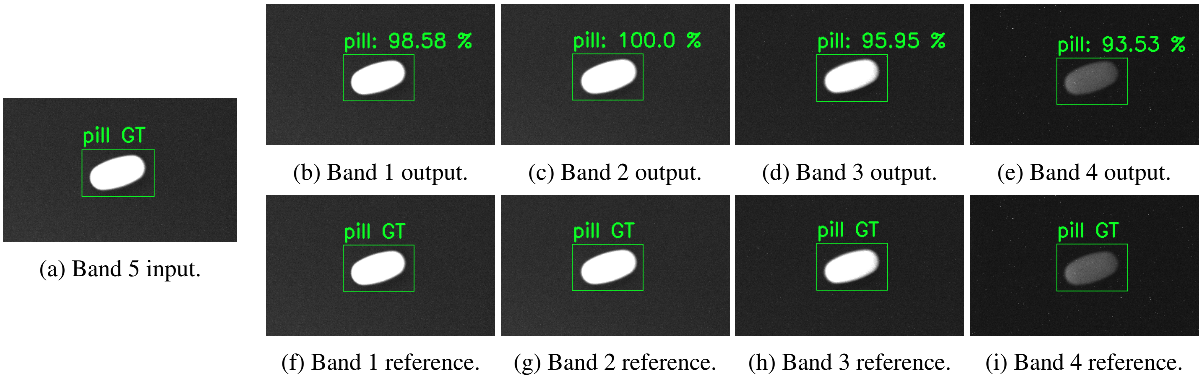

(a) Band 5 input. (b) Band 1 output. (c) Band 2 output. (d) Band 3 output. (e) Band 4 output. (f) Band 1 reference. (g) Band 2 reference. (h) Band 3 reference. (i) Band 4 reference.

Figure 2: BB labeled experiment: (a) Reference image (band 5) to start with, (b, c, d, e) Transformed labels (bands 1-4) and (f, g, h, i) Ground truth labels for comparison purposes (bands 1-4).

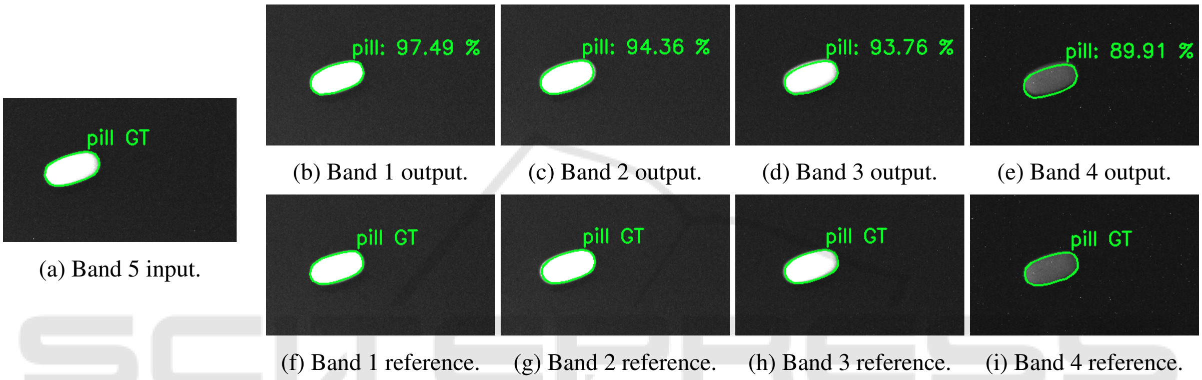

(a) Band 5 input. (b) Band 1 output. (c) Band 2 output. (d) Band 3 output. (e) Band 4 output. (f) Band 1 reference. (g) Band 2 reference. (h) Band 3 reference. (i) Band 4 reference.

Figure 3: Mask labeled experiment: (a) Reference image (band 5) to start with, (b, c, d, e) Transformed labels (bands 1-4) and (f, g, h, i) Ground truth labels for comparison purposes (bands 1-4).

$$\begin{aligned} l_{band1} &= \tfrac{1}{5}\,\mathrm{T}_{BB|mask} \cdot l_{RGB} \\ l_{band2} &= \tfrac{2}{5}\,\mathrm{T}_{BB|mask} \cdot l_{RGB} \\ l_{band3} &= \tfrac{3}{5}\,\mathrm{T}_{BB|mask} \cdot l_{RGB} \\ l_{band4} &= \tfrac{4}{5}\,\mathrm{T}_{BB|mask} \cdot l_{RGB} \\ l_{band5} &= I_{2x3} \cdot l_{RGB} \end{aligned} \tag{10}$$

The initial process for generating the $im_{RGB} = [R,G,B]$ is illustrated in Fig. 4. A combination of blue (Fig. 4a), green (Fig. 4b) and red (Fig. 4c) images is performed, generating the artificial fake RGB image (Fig. 4d).

Once the artificial RGB image has been generated, the objects have been labeled in both the BB format (Fig. 5a) and the mask format (Fig. 6a). Subsequently, the images with BB (Figs. 5b-5f) and masks (Figs. 6b-6f) were generated by applying the transformations obtained from Section 3.2. As it can be observed, the results obtained demonstrate the efficacy of the proposed approach. For instance, the objects in band 4 with BB (Fig. 5e) and mask (Fig. 6e) labeling are no longer visible to some extent. However, due to the method designed, the objects in those positions are labeled even though they are not visible.

4 CONCLUSION

This work presents a method for automatically labelling multispectral images, beginning with a single-band image BB or mask labeled image.

In order to achieve this, a two-step process is employed, comprising phase correlation and refinement. In the initial step, the transformation between the two images is obtained by applying a Hanning window to the image, transforming the spatial domain images into the frequency domain with the Fourier discrete transform, applying the cross-power spectrum formula to retain just the phase information of the images, converting the cross-power spectrum back to the spatial domain, and finally locating the peak, which represents the translation between the two analysed images. The second process entails refining the transformation obtained in the preceding step by searching

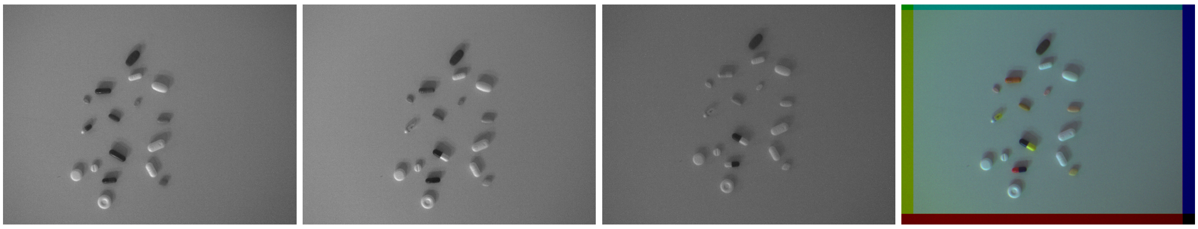

(a) Band 1: blue.

(b) Band 2: green.

(c) Band 3: red.

(d) Fake RGB image.

Figure 4: Combination to create fake RGB images: (a,b,c) Bands 1, 2, 3, respectively and (d) Generated fake RGB image.

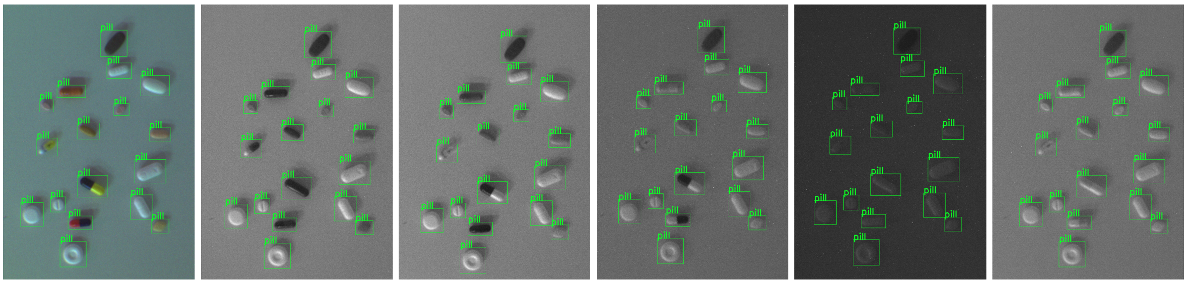

(a) Fake RGB labeled with BBs.

(b) Band 1 with transfered labels.

(c) Band 2 with transfered labels.

(d) Band 3 with transfered labels.

(e) Band 4 with transfered labels.

(f) Band 5 with transfered labels.

Figure 5: BB labeled fake RGB image and transferred labels: (a) Fake RGB image with BB labels and (b,c,d,e,f) Labels transferred to bands 1-5, respectively.

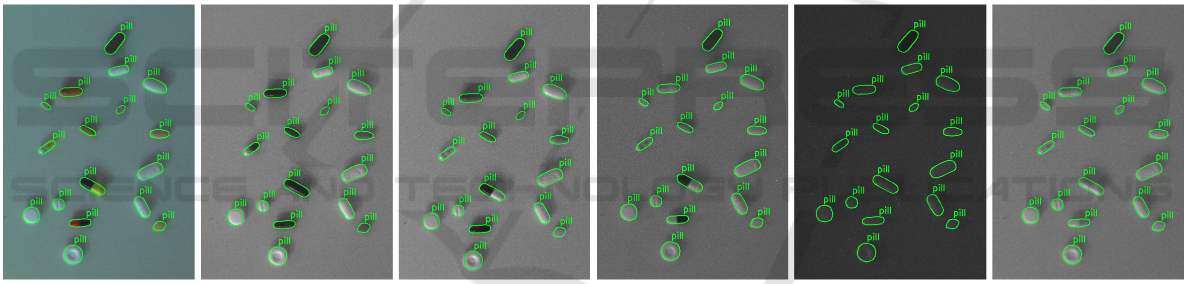

(a) Fake RGB labeled with masks.

(b) Band 1 with transfered labels.

(c) Band 2 with transfered labels.

(d) Band 3 with transfered labels.

(e) Band 4 with transfered labels.

(f) Band 5 with transfered labels.

Figure 6: Mask labeled fake RGB image and transferred labels: (a) Fake RGB image with mask labels and (b,c,d,e,f) Labels transferred to bands 1-5, respectively.

in a proximity window for an optimal one through an iterative process at the pixel and two subpixel levels, with the best transformation being saved as the one that yielded the highest percentage in the IOU index.

In order to test the method, the transformation between five multispectral lenses from a MicaSense RedEdge-MX Dual camera was obtained. By simply labeling 12 images from band 5 with a high contrast, it was possible to obtain the transformation of the label types with an accuracy of 97% and 94% for the BB and mask label types, respectively, in just 58 ms and 72 ms. Subsequently, the inverse of the aforementioned transformations was employed to generate an artificial RGB image, thereby facilitating the labelling process in coloured images. Subsequently, the labels are transformed back into each lens, thus ensuring that the labels are present in all five channels of the multispectral camera.

Future work will include testing the proposed method on additional multispectral cameras with differing morphologies, as well as testing it with all ten lenses that the camera used in the present paper has. Furthermore, the integration of an RGB camera would facilitate the avoidance of the generation of artificial RGB images derived from the multispectral lenses, thereby reducing the potential for the accumulation of minor errors during the process. An alternative approach would be to create a dataset of domestic waste with the aim of training different NNs and testing whether the additional information provided by 10 lenses and 12-bit images could facilitate more accurate categorisation compared to the same NNs using 8-bit RGB images of objects that resemble the same but are made of different materials.

ACKNOWLEDGEMENTS

Research work was funded by grant PID2021-122685OB-I00 funded by MICIU/AEI/10.13039/501100011033 and ERDF/EU.

REFERENCES

Andersson, P., Montan, S., and Svanberg, S. (1987). Multispectral system for medical fluorescence imaging. *IEEE Journal of Quantum Electronics*, 23(10):1798–1805.

Benjamin, MatvL, midaha, PGibson, RMcKinlay, and Kan, W. (2016). Dstl satellite imagery feature detection.

Gallagher, J. E., Gogia, A., and Oughton, E. J. (2024). A multispectral automated transfer technique (matt) for machine-driven image labeling utilizing the segment anything model (sam). *arXiv preprint*.

Gómez, P. and Meoni, G. (2021). Msmatch: Semisupervised multispectral scene classification with few labels. *IEEE Journal of Selected Topics in Applied Earth Observations and Remote Sensing*, 14:11643–11654.

Helber, P., Bischke, B., Dengel, A., and Borth, D. (2019). Eurosat: A novel dataset and deep learning benchmark for land use and land cover classification. *IEEE Journal of Selected Topics in Applied Earth Observations and Remote Sensing*, 12(7):2217–2226.

Hoffer, R., Johannsen, C., and Baumgardner, M. (1966). Agricultural applications of remote multispectral sensing. In *Proceedings of the Indiana Academy of Science*, volume 76, pages 386–396.

Kemker, R., Salvaggio, C., and Kanan, C. (2018). Algorithms for semantic segmentation of multispectral remote sensing imagery using deep learning. *ISPRS Journal of Photogrammetry and Remote Sensing*.

Kirillov, A., Mintun, E., Ravi, N., Mao, H., Rolland, C., Gustafson, L., Xiao, T., Whitehead, S., Berg, A. C., Lo, W.-Y., et al. (2023). Segment anything. In *Proceedings of the IEEE/CVF International Conference on Computer Vision*, pages 4015–4026.

Lowe, D. G. (1999). Object recognition from local scale-invariant features. In *Proceedings of the seventh IEEE international conference on computer vision*, volume 2, pages 1150–1157. IEEE.

Ma, F., Yuan, M., and Kozak, I. (2023). Multispectral imaging: Review of current applications. *Survey of Ophthalmology*, 68(5):889–904.

Maxwell, E. L. (1976). Multivariate system analysis of multispectral imagery. *Photogrammetric Engineering and Remote Sensing*, 42(9):1173–1186.

Mia, M. S., Tanabe, R., Habibi, L. N., Hashimoto, N., Homma, K., Maki, M., Matsui, T., and Tanaka, T. S. T. (2023). Multimodal deep learning for rice yield prediction using uav-based multispectral imagery and weather data. *Remote Sensing*, 15(10).

Ošep, A., Meinhardt, T., Ferroni, F., Peri, N., Ramanan, D., and Leal-Taixé, L. (2024). Better call sal: Towards learning to segment anything in lidar. *arXiv preprint*.

Páez-Ubieta, I. d. L., Castaño-Amorós, J., Puente, S. T., and Gil, P. (2023). Vision and tactile robotic system to grasp litter in outdoor environments. *Journal of Intelligent & Robotic Systems*, 109(2):36.

Park, H. G., Yun, J. P., Kim, M. Y., and Jeong, S. H. (2021). Multichannel object detection for detecting suspected trees with pine wilt disease using multispectral drone imagery. *IEEE Journal of Selected Topics in Applied Earth Observations and Remote Sensing*, 14:8350–8358.

Páez-Ubieta, I. d. L., Velasco-Sánchez, E., Puente, S. T., and Candelas, F. (2023). Detection and depth estimation for domestic waste in outdoor environments by sensors fusion. *IFAC-PapersOnLine*, 56(2):9276–9281. 22nd IFAC World Congress.

Torralba, A., Russell, B. C., and Yuen, J. (2010). Labelme: Online image annotation and applications. *Proceedings of the IEEE*, 98(8):1467–1484.

Ulku, I., Akagündüz, E., and Ghamisi, P. (2022). Deep semantic segmentation of trees using multispectral images. *IEEE Journal of Selected Topics in Applied Earth Observations and Remote Sensing*, 15:7589–7604.

Wang, C.-Y., Bochkovskiy, A., and Liao, H.-Y. M. (2023). Yolov7: Trainable bag-of-freebies sets new state-of-the-art for real-time object detectors. In *2023 IEEE/CVF Conference on Computer Vision and Pattern Recognition (CVPR)*, pages 7464–7475. IEEE.

Wang, X., Zhang, R., Kong, T., Li, L., and Shen, C. (2020). Solov2: Dynamic and fast instance segmentation. *Advances in Neural information processing systems*, 33:17721–17732.

Yang, Y. and Newsam, S. (2010). Bag-of-visual-words and spatial extensions for land-use classification. In *Proceedings of the 18th SIGSPATIAL international conference on advances in geographic information systems*, pages 270–279.

Yuan, K., Zhuang, X., Schaefer, G., Feng, J., Guan, L., and Fang, H. (2021). Deep-learning-based multispectral satellite image segmentation for water body detection. *IEEE Journal of Selected Topics in Applied Earth Observations and Remote Sensing*, 14:7422–7434.